Assimilating All-Sky Himawari-8 Satellite Infrared Radiances: A Case of Typhoon Soudelor (2015)

Honda, Takumi ; Miyoshi, Takemasa ; Lien, Guo-Yuan ; Nishizawa, Seiya ; Yoshida, Ryuji ; Adachi, Sachiho A. ; Terasaki, Koji ; Okamoto, Kozo ;…

(Citation)
Monthly Weather Review,146(1):213-229

(Issue Date)
2018-01-17

(Resource Type)
journal article

(Version)
Version of Record

(URL)
https://hdl.handle.net/20.500.14094/90004548

Assimilating All-Sky *Himawari-8* Satellite Infrared Radiances: A Case of Typhoon Soudelor (2015)

TAKUMI HONDA,[a] TAKEMASA MIYOSHI,[b] GUO-YUAN LIEN,[a] SEIYA NISHIZAWA,[a] RYUJI YOSHIDA,[a] SACHIHO A. ADACHI,[a] KOJI TERASAKI,[a] KOZO OKAMOTO,[c] HIROFUMI TOMITA,[a] AND KOTARO BESSHO[d,e]

[a] *RIKEN Advanced Institute for Computational Science, Kobe, Japan*
[b] *RIKEN Advanced Institute for Computational Science, Kobe, Japan, and Department of Atmospheric and Oceanic Science, University of Maryland, College Park, College Park, Maryland, and Japan Agency for Marine-Earth Science and Technology, Yokohama, Japan*
[c] *Meteorological Research Institute, Japan Meteorological Agency, Tsukuba, and RIKEN Advanced Institute for Computational Science, Kobe, Japan*
[d] *Meteorological Satellite Center, Japan Meteorological Agency, Kiyose, Japan*

(Manuscript received 15 September 2016, in final form 18 November 2017)

ABSTRACT

Japan's new geostationary satellite *Himawari-8*, the first of a series of the third-generation geostationary meteorological satellites including *GOES-16*, has been operational since July 2015. *Himawari-8* produces high-resolution observations with 16 frequency bands every 10 min for full disk, and every 2.5 min for local regions. This study aims to assimilate all-sky every-10-min infrared (IR) radiances from *Himawari-8* with a regional numerical weather prediction model and to investigate its impact on real-world tropical cyclone (TC) analyses and forecasts for the first time. The results show that the assimilation of *Himawari-8* IR radiances improves the analyzed TC structure in both inner-core and outer-rainband regions. The TC intensity forecasts are also improved due to *Himawari-8* data because of the improved TC structure analysis.

1. Introduction

Despite the recent progress in numerical weather prediction (NWP), accurately forecasting tropical cyclones (TCs) is a big challenge, especially because of their intensity change (DeMaria et al. 2014; National Hurricane Center 2016). Data assimilation (DA) plays a key role in the effective use of available observations to obtain better initial conditions and to improve the subsequent forecasts in NWP. TCs usually spend most of their life span over the ocean, where in situ observations are generally limited. Therefore, improving DA of precious observations over the ocean from satellites and aircraft could be important for the TC forecasts. A number of studies have explored ways to improve TC forecasting by using various observation data; for example, Miyoshi and Kunii (2012) with the satellite-borne Atmospheric Infrared Sounder (AIRS) retrieval data, Wu et al. (2012) with dropwindsonde data, Zhang and Weng (2015) with airborne Doppler radar observations, and Zou et al. (2015) with clear-sky radiances from the *GOES-13* and *GOES-15* geostationary satellites operated by the National Oceanic and Atmospheric Administration (NOAA).

Geostationary satellites can observe a wide area frequently, and are effective at observing TCs over the ocean. In fact, geostationary satellites can capture a rotating cluster of convective clouds associated with TCs and have long been playing a crucial role in analyzing the TC best track data at the weather services (e.g., Velden et al. 2006). However, assimilating all-sky infrared (IR) radiances in NWP is still a major challenge. For example, cloud resolving model simulation requires a large computational resource, includes highly nonlinear processes (Bauer et al. 2011), and could be affected by the choice of parameterization

Denotes content that is immediately available upon publication as open access.

[e] Current affiliation: Forecast Department, Japan Meteorological Agency, Tokyo, Japan.

Corresponding author: Takumi Honda, takumi.honda@riken.jp

DOI: 10.1175/MWR-D-16-0357.1

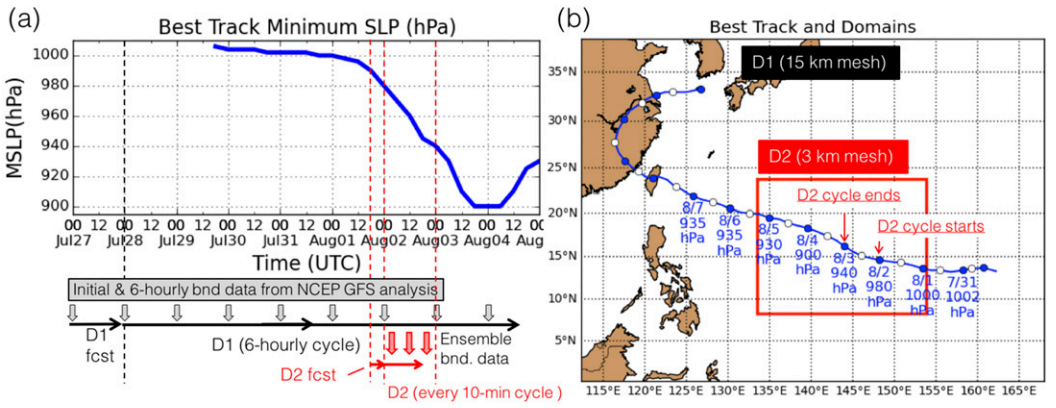

FIG. 1. (a) Evolution of the best track minimum sea level pressure (MSLP; hPa) of Typhoon Soudelor (2015) and experimental flows (black and red arrows). (b) The computational domains and best track of Typhoon Soudelor (2015). The figure frame and red rectangle correspond to the 15-km-mesh parent (D1) and 3-km-mesh daughter (D2) domains, respectively. The open and closed blue circles show 12-hourly positions of Typhoon Soudelor (2015) at 0000 and 1200 UTC from JMA best track data, respectively. JMA best track data are available at http://www.jma.go.jp/jma/jma-eng/jma-center/rsmc-hp-pub-eg/besttrack.html.

schemes (Otkin et al. 2017). Simulating satellite observations from model output via a forward radiative transfer model (RTM) has a large uncertainty (Okamoto 2017). Moreover, satellite radiances often contain correlated errors among different frequency bands (Bormann et al. 2010, 2016), so that assimilating multiple bands at the same time is not straightforward. Furthermore, it is unclear how to estimate and correct the bias effectively. Although the bias-correction procedure for the global-scale satellite radiance DA from low-Earth orbiters has been addressed by many previous studies (e.g., Derber and Wu 1998; Fertig et al. 2009; Miyoshi et al. 2010), the procedure for cloud-resolving regional DA with frequent radiance observation from the geostationary orbit has not been well established. Recently, Lin et al. (2017) applied a bias-correction procedure for satellite radiance observations with NOAA's operational Rapid Refresh (RAP) hourly updating system at 13-km resolution, but this study focuses on a more frequently updating high-resolution system.

Recently, Zhang et al. (2016) tackled this tough problem of assimilating all-sky IR radiances by conducting an observing system simulation experiment (OSSE) for a TC case. They showed that TC analyses and forecasts were dramatically improved through the assimilation of simulated NOAA's new-generation geostationary satellite GOES-R (now *GOES-16*, launched in November 2016) radiances at high spatiotemporal resolution of every 10 min under all-sky conditions. They demonstrated significant improvements in both radar reflectivity and wind field of a simulated TC case by using the all-sky radiances. They further performed an experiment with real IR observations from *GOES-13* and showed benefits of all-sky radiance DA.

In July 2015, the Japan Meteorological Agency (JMA) started full operations of the new geostationary satellite *Himawari-8* (Bessho et al. 2016), the first of a series of the third-generation geostationary meteorological satellites including *GOES-16*. Advanced Himawari Imager (AHI) on board *Himawari-8* produces high-resolution observations with 16 frequency bands every 10 min for full disk, and every 2.5 min for local regions fixed around Japan and adaptive around typhoons. In August 2015, *Himawari-8* successfully captured the rapid intensification of Typhoon Soudelor (2015), the strongest western North Pacific TC in 2015 reaching the minimum sea level pressure (MSLP) of 900 hPa (Fig. 1a).

Following the promise shown by Zhang et al. (2016) with the simulated GOES-R radiance data, the present study aims to assimilate the real-world *Himawari-8* all-sky IR radiances for the case of Typhoon Soudelor (2015) and to investigate its impact on the analyses and forecasts. Several studies have investigated characteristics of the *Himawari-8* observations (Zou et al. 2016) and their impacts on precipitation forecast (Honda et al. 2018; Qin et al. 2017), but this is the first study published thus far showing the *potential* of every-10-min IR radiances in NWP for a real-world typhoon case. Section 2 describes the experimental design. Section 3 presents the results and discussion. Section 4 provides the summary.

2. Methodology

We use the system developed by Lien et al. (2017, hereafter L17), who combined a regional model from the scalable computing for advanced library and environment (SCALE; Nishizawa et al. 2015; Sato et al. 2015)

library, or simply SCALE-RM, with the local ensemble transform Kalman filter (LETKF; Hunt et al. 2007; Miyoshi and Yamane 2007) to create SCALE-LETKF. The SCALE-RM is set up with two domains located in the western North Pacific region; namely, a 3-km-mesh daughter domain (hereafter D2) with $720 \times 576 \times 56$ grid points is nested within a 15-km-mesh parent domain (hereafter D1) with $384 \times 288 \times 36$ grid points (Fig. 1b). Here, the nesting is one way, so that D1 provides the boundary conditions for D2, but D2 does not affect D1. We first run the entire period of the D1 DA experiment, followed by the D2 DA experiments. The model tops for D1 and D2 are 27.7 and 26.6 km, respectively. The Tomita (2008) single-moment bulk microphysics scheme is used in both D1 and D2. To represent subgrid-scale turbulences, we apply the level-2.5 closure of the Mellor–Yamada–Nakanishi–Niino turbulence scheme (Nakanishi and Niino 2004). Shortwave and longwave radiation processes are parameterized by Model Simulation Radiation Transfer code (MSTRN) X (Sekiguchi and Nakajima 2008). A Beljaars-type bulk surface-flux model (Beljaars and Holtslag 1991) and a single-layer urban canopy model (Kusaka et al. 2001) are used. The 6-hourly boundary conditions including sea surface temperature are given by the National Centers for Environmental Prediction (NCEP) Global Forecast System (GFS) analysis data with 0.5° horizontal resolution.

In this study, the ensemble size is fixed at 50. The 6-hourly DA cycle for D1 is initiated at 0000 UTC 28 July 2015 after a 1-day spinup of ensemble forecasts (Fig. 1a). Following L17, the initial ensemble for D1 is created from the 0.5° NCEP GFS analysis data at 0000 UTC of arbitrarily chosen dates in July 2013 and 2014. Verifying against the NCEP GFS analyses, we confirmed that the D1 DA cycle spins up sufficiently within 4 days, before initiating the D2 DA cycle. Other DA settings for D1 follow the near-real-time system developed by L17. Namely, the LETKF for D1 assimilates the 6-hourly conventional (nonradiance) NCEP PREPBUFR observations. In both D1 and D2 DA cycles, covariance localization is applied by a Gaussian function but forced to be zero beyond $2\sqrt{10/3}$ standard deviation. The localization scales, defined by the standard deviation of the Gaussian function, are chosen to be 400 km horizontally and 0.3 vertically in the natural logarithmic pressure ($\ln p$) coordinate, following L17.

Since the boundary conditions for D1 are the same among all ensemble members, the ensemble spread is zero at the boundaries. Therefore, we need to carefully design covariance inflation for D1. L17 tested several methods and tunable parameters, and concluded that a combination of multiplicative covariance inflation and relaxation to prior perturbation (RTPP; Zhang et al. 2004) can keep the ensemble spread in a reasonable range even with a fixed boundary condition and a limited domain size. Here we follow L17 for D1 and apply multiplicative inflation to the background error covariance with a constant factor of 2.0, followed by RTPP with the relaxation constant of 0.8. The relatively large multiplicative inflation by a factor of 2.0 is required to keep the ensemble spread sufficiently large.

The D2 DA cycle is conducted every 10 min with initial and boundary data given by the D1 cycle. The D2 cycle is initiated at 0000 UTC 2 August 2015 after 6-h spinup ensemble forecasts and ends at 0000 UTC 3 August 2015 (Fig. 1a). For the D2 cycle, we apply only RTPP with a slightly larger relaxation constant of 0.85. A different relaxation constant of 0.90 was also tested, but the results were not improved. Since the D1 cycle provides the ensemble boundary conditions, multiplicative inflation is not used.

We assimilate three types of observations for the D2 cycle: PREPBUFR, TC vital data (MSLP and TC position), and *Himawari-8* radiances. The 6-hourly PREPBUFR observations are split into every-10-min bins. The horizontal localization scale for the PREPBUFR observations is set to be 50 km, similar to 50–100-km adaptive localization of the German Weather Service's Kilometer-Scale Ensemble Data Assimilation (KENDA) system with a 2.8-km horizontal grid spacing (Schraff et al. 2016). The vertical localization scale for the PREPBUFR observations is chosen to be the same as those of the D1 cycle. The TC vital data are assimilated every hour using the TC vital observation operator that searches the center position and intensity (MSLP) of TCs in the background ensemble (Chen and Snyder 2007). Here, we do not apply a TC relocation technique (Hsiao et al. 2010) although recently Nehrkorn et al. (2015) reported an advanced technique to correct the TC position errors. The hourly TC vital data are linearly interpolated from the 6-hourly JMA best track data, as in Heming (2016). Zhang et al. (2016) also assimilated hourly TC vital data in their simulation experiments. Previous studies estimated the uncertainty of the TC vital observation (e.g., Torn and Snyder 2012; Kleist 2011; Holt et al. 2015; Heming 2016). As noted by Zhang et al. (2016), high-spatiotemporal resolution data by *Himawari-8* and GOES-R would improve the accuracy of the TC vital observation, but the validation data are not yet available. Therefore, we simply follow Torn (2010) and Kunii (2015) and assume that the observation error standard deviations for the intensity (MSLP) and position are 3 hPa and 20 km, respectively. The horizontal localization scales for the TC vital data are chosen to be 200 km, similar to Kunii (2015) and Wu et al. (2010).

Vertical localization is not applied for the TC vital observation.

We assimilate every-10-min full disk scan observations from *Himawari-8* using an RTM known as the RTTOV11.2 (Saunders et al. 2013) as the observation operator. First, we convert the Himawari Standard Data (HSD; Bessho et al. 2016) with count values of each pixel to gridded Network Common Data Form (NetCDF) data at 0.20° × 0.20° horizontal resolution by using the nearest pixel values at each grid point. This is equivalent to thinning. Next, the data are converted to binary observation input data for the LETKF. Although *Himawari-8* provides 10 IR band observations, we assimilate only band 9 (6.9 μm) as the first step to avoid potential complications with observation error correlations among different IR bands (e.g., Bormann et al. 2010, 2016). Recently, Okamoto (2017) compared the real *Himawari-8* observation with its simulation equivalent from a mesoscale cloud-resolving model and pointed out that moisture-sensitive bands have more suitable characteristics such as the Gaussian probability distribution function (PDF) than window bands. Among the three water vapor bands (bands 8, 9, and 10; Bessho et al. 2016), in clear-sky conditions, band 8 (6.2 μm) is sensitive to the upper troposphere, band 9 (6.9 μm) is sensitive to the upper to midtroposphere, and band 10 (7.3 μm) is sensitive to the midtroposphere (Otkin 2012). Here we use band 9, which is expected to have intermediate characteristics among the three water vapor bands.

Since the TC position error would be relatively large at an earlier stage of the D2 DA cycles, we do not assimilate the *Himawari-8* observation during the first six cycles of the D2 DA experiment (1 h). At the sixth cycle, the first TC vital DA would reduce the TC position error, so that we start assimilating the *Himawari-8* observation from the seventh analysis at 0110 UTC 2 August 2015.

We apply a simple method for diagnosing the observation error standard deviations for the *Himawari-8* radiances separately for each sky condition (i.e., clear sky and cloudy sky). Here, the sky condition is diagnosed by using the cloud effect average C_A developed by Okamoto et al. (2014): $C_A = (|C_M| + |C_O|)/2$, where $C_M(=B - B_{\rm clr})$ denotes the cloud effect on the model, and $C_O(=O - B_{\rm clr})$ the cloud effect on the observation. Here, B and $B_{\rm clr}$ denote all-sky and clear-sky first-guess brightness temperatures, respectively, and O denotes the observation. The term $B_{\rm clr}$ is derived from RTTOV without the cloud-scattering calculation. We compute C_A for band 9, the directly assimilated band. Here, we categorize the innovation samples into the clear-sky and cloudy-sky conditions by using a threshold of $C_A = 1.0$. Since a small C_A value corresponds to a smaller impact by clouds, the *Himawari-8* observations with $C_A \le 1.0$ are regarded as clear-sky (cloud free) observations. Harnisch et al. (2016) pointed out that clear-sky samples diagnosed by $C_A \le 1.0$ exhibit similar characteristics with cloud-free samples independently diagnosed by liquid and ice water contents. In clear-sky conditions, the observation error standard deviation is set to be 3 K, similar to Otkin (2012) and Zhang et al. (2016), whereas it was inflated by a factor of 2 in the cloudy-sky condition (6 K), by considering large uncertainty in the cloudy-sky condition (e.g., Okamoto et al. 2014; Okamoto 2017). The resulting observation error standard deviation is a step function of C_A and is a simplified form of the piecewise-linear function used by Okamoto (2017). We apply a simple gross-error check, so that the *Himawari-8* observations with a large departure from the model background by more than 15 K (5 times larger than the clear-sky observation error standard deviation) are rejected. The factor of 5 is the default value of SCALE-LETKF and the same as the L17 setting for other types of observations.

Regarding the horizontal localization scale σ_H for the *Himawari-8* radiances, a series of sensitivity experiments with different values of σ_H were performed. The tested values of σ_H are 20, 30, 40, 50, 60, and 70 km. We verified the performance of each experiment by comparing the TC forecasts, and concluded that $\sigma_H = 60$ km gave the best results. Therefore, in the next section, we mainly show the results with $\sigma_H = 60$ km. It is not straightforward to interpret this sensitivity because the best localization scale would depend on both ensemble size and correlation length scale. As shown by Zhang et al. (2016), the IR radiance observations can have long-range correlations associated with a TC. This partially explains why $\sigma_H = 60$ km (the radius of influence of about 219 km), close to the 200-km radius of influence of Zhang et al. (2016), was the best choice. The results of the sensitivity tests are also presented in section 3e.

As for the vertical localization for *Himawari-8* observations, the peak level of the clear-sky weighting function (CSWF) derived by the RTM and the ensemble mean of the cloud-top (CTP) height are considered to obtain the localization center. Here, the CTP height is defined as the highest grid point where the sum of the hydrometeor mass concentration except for rain (i.e., cloud water, cloud ice, snow, and graupel) is greater than or equal to 0.1 g m^{-3}. If the CSWF peak height is higher than the diagnosed CTP height, the Gaussian function centered at the CSWF peak is used (Houtekamer et al. 2005; Miyoshi and Sato 2007). Since Otkin (2012) pointed out that moisture-sensitive bands are affected by clouds located near or above the CSWF height, we

use the Gaussian function centered at the average height between the CSWF peak height and CTP height if the CTP height is higher than the CSWF peak height. Indeed, we analyzed the ensemble-based correlations between the model variables and simulated brightness temperature (not shown) and confirmed that large correlations can be located much higher than the CSWF peak height in deep convection areas. We also conducted sensitivity experiments for the vertical localization scale σ_V for the *Himawari-8* radiances, and found that the larger value of σ_V ($= 0.5 \ln p$) gives the better intensity forecast compared to the smaller value ($\sigma_V = 0.3 \ln p$). This is likely because the brightness temperature observation is often associated with deep convection with longer vertical correlation length scales (e.g., Zhang et al. 2016). Indeed, Lei and Whitaker (2015) demonstrated that large vertical localization scales are more suitable for effective radiance DA. Therefore, we use $\sigma_V = 0.5 \ln p$. A larger localization scale generally requires a larger ensemble size, and further sensitivity to $\sigma_V > 0.5$ is not tested.

As already mentioned in section 1, bias correction for cloud-resolving regional DA with frequent radiance observations has not been well established. In this study, we apply no bias correction, and will show in sections 3a and 3d that bias is very small even without bias correction when the *Himawari-8* observations are assimilated every 10 min in our case study.

To investigate the impact of *Himawari-8* DA, we compare the results of the following two experiments. The first experiment (hereafter labeled as "Him8") assimilates all of the three kinds of the observations (i.e., conventional, TC vital, and *Himawari-8* observations). The other experiment (hereafter labeled as "NoHim8") assimilates only the conventional and TC vital observations.

3. Results and discussion

a. Analyzed TC structure and innovation statistics

Assimilating *Himawari-8* radiance observations significantly improves the analyzed TC structure. Figure 2 presents horizontal maps *of Himawari-8* radiances simulated from the analyses and actual observation at band 13 (10.4 μm), a window band. Although the *Himawari-8* observation at band 13 is not assimilated directly, Him8 successfully captures the major patterns of the observed TC structure, particularly, the outer rainbands located in the northern and southwestern regions.

To demonstrate that the assimilation of *Himawari-8* IR observations works correctly, we compute the innovation statistics for each sky condition (i.e., clear sky, cloudy sky, and all sky). The sky condition is diagnosed by the same threshold of $C_A = 1$ as that used for the observation error diagnosis. Figure 3 shows the probability density functions (PDFs) of the O-minus-B innovations ($O - B$) and the O-minus-analysis innovations ($O - A$). Samples are collected from 0310 to 0600 UTC 2 August, totaling 18 DA cycles. The standard deviation for the all-sky samples is reduced by DA, indicating that the *Himawari-8* DA works correctly. As expected, the standard deviation for the cloudy sky is larger than that for the clear sky, resulting in an intermediate value of the standard deviation for the all-sky samples. We discuss the bias in section 3d. As pointed out by Okamoto et al. (2014) and Harnisch et al. (2016), the PDFs in the cloudy-sky and all-sky conditions have more non-Gaussian distributions than in the clear-sky condition.

Here, we further verify the performance of *Himawari-8* DA. Figure 4 shows time series of the root-mean-square error (RMSE) and bias relative to the *Himawari-8* observations for several bands. After starting *Himawari-8* DA at 0110 UTC 2 August 2015, the RMSE for band-9 brightness temperature quickly decreases and becomes stationary albeit a slight increase in a later period likely associated with the intensification of the TC. This trend is also the case for different bands, indicating that assimilating band 9 also improves different moisture and window bands that are not directly assimilated. After several DA cycles, bias becomes small and fluctuates around zero, likely due to frequent DA. Bias correction is essential in the global-scale DA with polar-orbiting satellite observations. However, in the regional-scale DA with very frequent geostationary satellite observations, the results of this single case study imply that bias correction and its importance could be different from the global-scale DA. This does not imply reduced importance of bias correction. Even with a small bias in the regional-scale DA, bias would certainly degrade the analysis and had better be removed. To extract the full potential of the *Himawari-8* IR observations, it is essential to apply bias correction. Here we limit ourselves to investigating the impact of assimilating bias uncorrected *Himawari-8* radiances as the first step. Further improvements are expected in the future with proper bias correction.

As mentioned in section 2, we thinned out the original *Himawari-8* observations into 0.20° × 0.20° horizontal resolution. To confirm that the observation error correlation becomes sufficiently low as the distance increases, we carry out an additional 12 DA cycles for 2 h from 0100 UTC 2 August 2015 with high-resolution (0.04° × 0.04°) *Himawari-8* observation. Here we use the high-resolution observation to increase the sample size

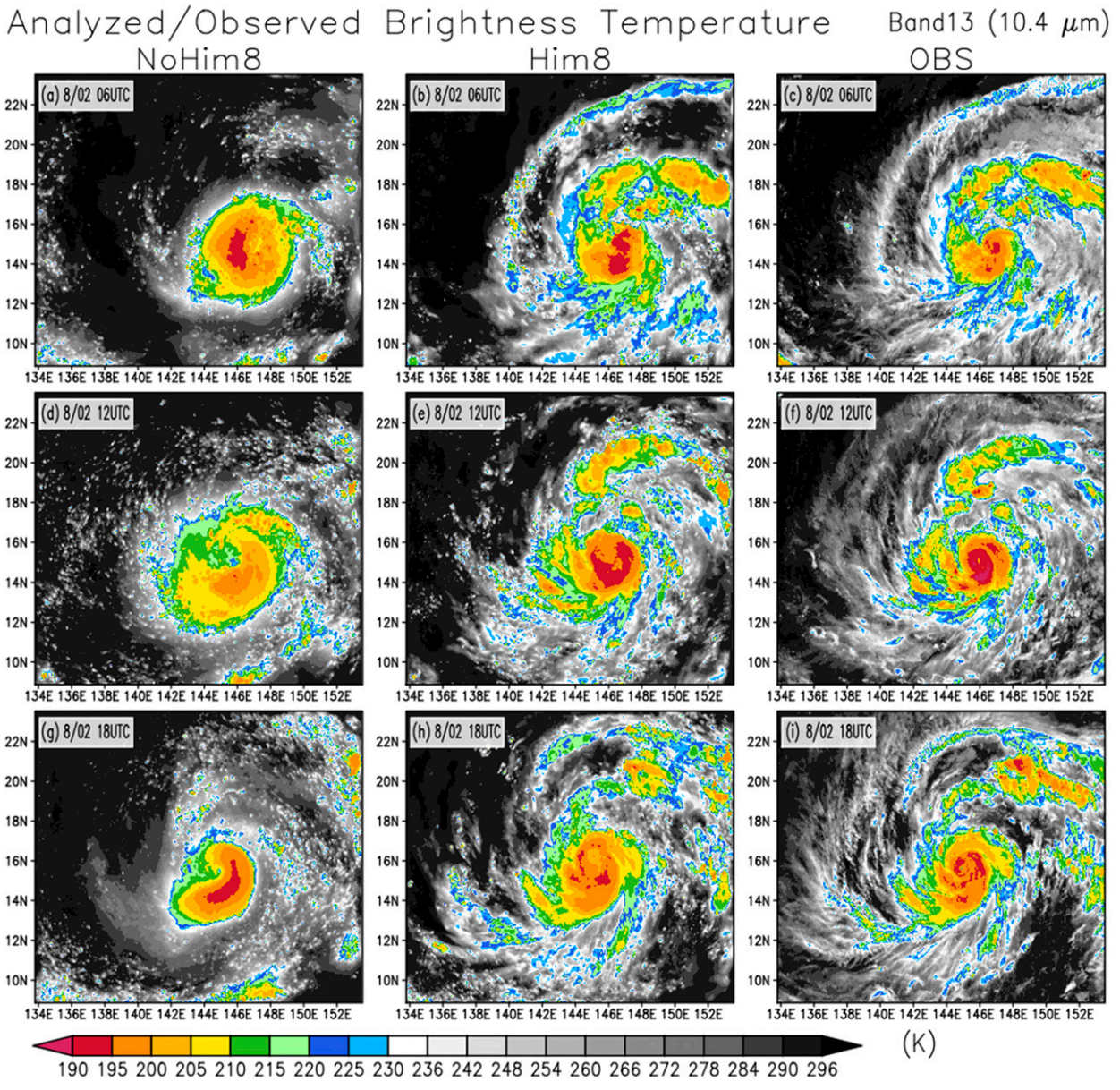

FIG. 2. Horizontal maps of *Himawari-8* brightness temperature (K) of band 13 (10.4 μm) at (a)–(c) 0600 UTC 2 Aug, (d)–(f) 1200 UTC 2 Aug, and (g)–(i) 1800 UTC 3 Aug. (a),(d),(g) NoHim8 ensemble mean analyses; (b),(e),(h) Him8 ensemble mean analyses; and (c),(f),(i) *Himawari-8* observations.

for better statistics. The additional DA cycle is also initialized by the NoHim8 ensemble analysis. Using the innovation samples collected from the third analysis (0130 UTC 3 August) to the ninth analysis (0230 UTC 3 August), we compute the innovation statistics of Desroziers et al. (2005). Figure 5a shows the estimated observation error correlations as a function of the distance. The observation error correlation becomes lower than 0.2 if the distance is larger than 0.20°, indicating that thinning can avoid potential problems caused by the horizontal observation error correlation. In addition, the statistics can estimate the observation error standard deviations; the estimated values are 3.89 K for all sky, 4.47 K for cloudy sky, and 0.55 K for clear sky. However, the Desroziers statistics tend to underestimate the observation error standard deviation, so that we often need to use a larger value in data assimilation (Campbell et al. 2017). Our setting (i.e., 3 K for clear sky and 6 K for cloudy sky) is larger than the Desroziers statistics; we do not further tune these values here.

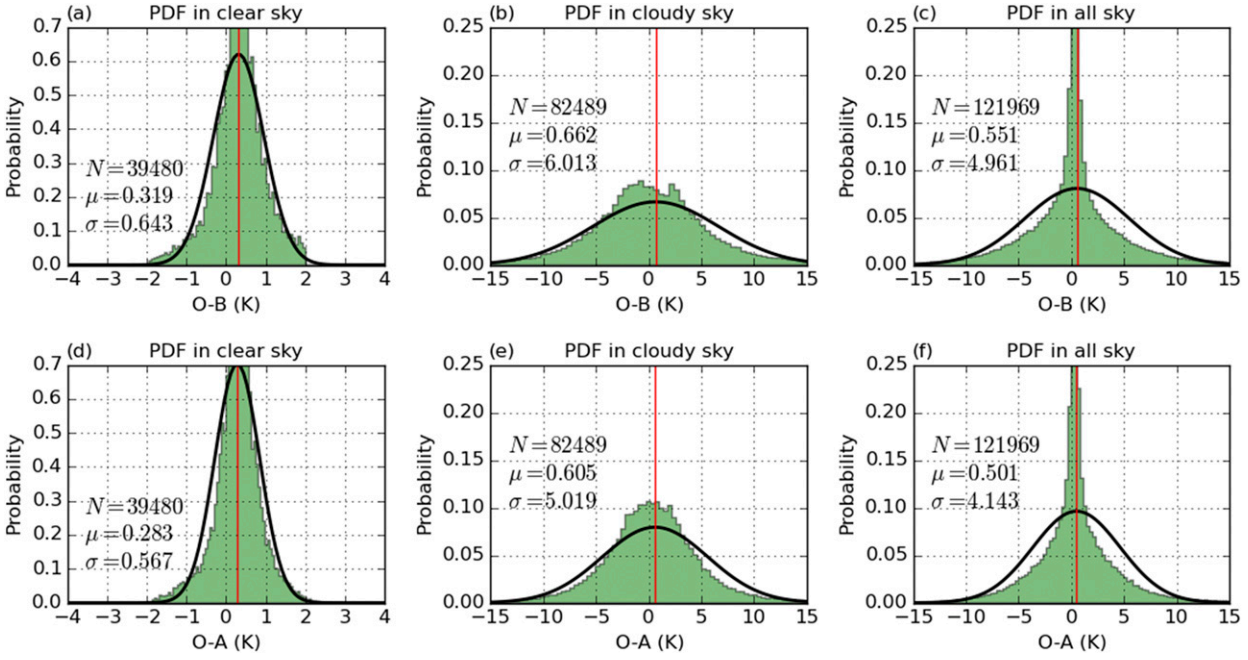

FIG. 3. Probability density function (PDF) of (a)–(c) observation-minus-background ($O - B$, innovation) and (d)–(f) observation-minus-analysis ($O - A$) for *Himawari-8* observation in (a),(d) clear-sky; (b),(e) cloudy-sky; and (c),(f) all-sky conditions, respectively. The sample size N, mean μ (shown by red lines), and standard deviation σ for each sample are presented in each panel. Black lines indicate Gaussian PDFs with μ and σ in each sample. The samples are collected from the 19th analysis (0310 UTC 2 Aug) to the 36th analysis (0600 UTC 2 Aug).

As mentioned in section 2, we assimilated only band 9 because of high observation error correlations between different moisture-sensitive bands. To estimate the observation error correlations by the innovation statistics of Desroziers et al. (2005), we conduct an additional short-period DA experiment until 0600 UTC 2 August assimilating bands 8, 9, and 10 at the same time without accounting for observation error correlations. To reduce the influence of spatial observation error correlations, the *Himawari-8* observations are thinned out to 0.20° × 0.20° horizontal resolution. Following Bormann et al. (2016), the diagnosed matrix is symmetrized by averaging with its transposed matrix. Figure 5b presents the estimated interband error correlations, which are generally high. The analyses in this experiment are generally degraded compared to Him8 (not shown). To effectively assimilate these bands at the same time, it is necessary to explicitly include the interband error correlations in data assimilation (e.g., Bormann et al. 2016; Campbell et al. 2017). This remains to be a subject of future research.

The distribution of hydrometeors is also improved by *Himawari-8* radiance DA. Here, we conduct a qualitative comparison with an independent observation. Figure 6 shows the horizontal patterns of the analyzed hydrometeors and an independent microwave satellite observation. We find a clear difference in the outer rainband, particularly in the northern region. Him8 shows a larger mixing ratio region around 20°N, consistent with the satellite microwave observation.

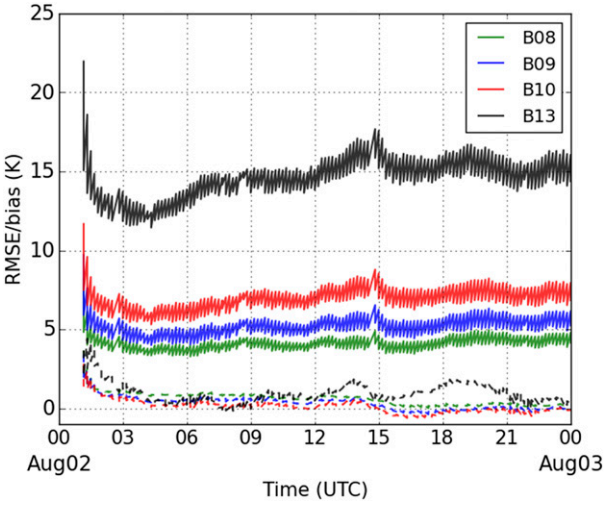

FIG. 4. Time series of the root-mean-square error (RMSE, solid curves) and bias (K, dashed curves) relative to the *Himawari-8* observation (K). Green, blue, red, and black curves correspond to band 8 (6.2 μm), band 9 (6.9 μm), band 10 (7.3 μm), and band 13 (10.4 μm), respectively.

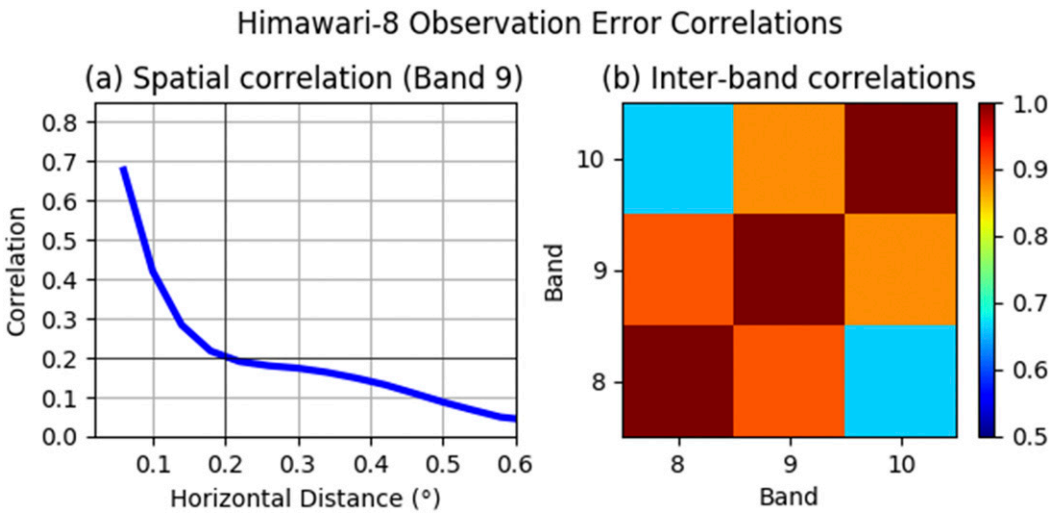

FIG. 5. (a) Estimated horizontal observation error correlations for *Himawari-8* observation (band 9). (b) Estimated interband observation error correlations among the *Himawari-8* moisture-sensitive bands (bands 8, 9, and 10).

This region corresponds to the area where the radiances are also improved (Figs. 2 and 6). This suggests that the all-sky radiance DA produce reasonable analysis increments of hydrometeors, as demonstrated by Zhang et al. (2016).

Here, we describe how assimilating the *Himawari-8* IR improves the analyzed clouds and convection. Figure 7 shows horizontal maps of the first guess, actual observation, and innovation, as well as zonal–vertical cross sections of the analysis increment. Positive (negative) analysis increments of hydrometeors and vertical velocity are found around region A (B) where the innovation is negative (positive). That is, *Himawari-8* DA enhances (suppresses) deep convection if the innovation is negative (positive). In general, deep convection stabilizes the atmosphere and is associated with latent heat release, so that the temperature analysis increment around point A is positive above the middle level (Fig. 7f). In addition, the water vapor analysis increment is positive around point A, because the induced convection around point A transports moisture to the free troposphere. On the other hand, around point B where the convection is suppressed by *Himawari-8* DA, a negative moisture increment is found.

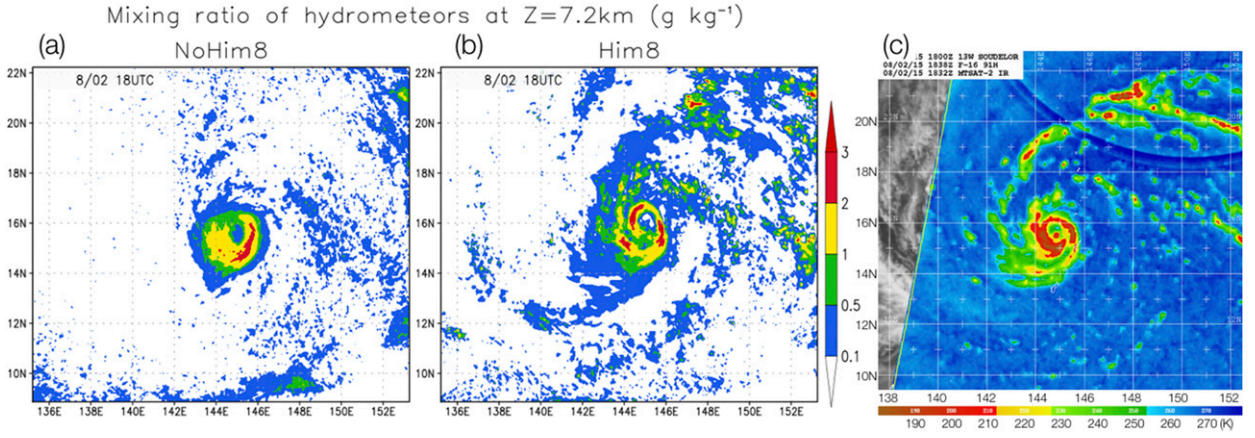

FIG. 6. (a),(b) Mixing ratio of hydrometeors (sum of cloud water, rain, cloud ice, snow, and graupel; g kg^{-1}) at $Z = 7.2$ km of the analysis ensemble mean in (a) NoHim8 and (b) Him8 at 1800 UTC 2 Aug. (c) Microwave satellite imagery [91H GHz on the Special Sensor Microwave Imager/Sounder (SSMIS) on board the Defense Meteorological Satellite Program (DMSP) *F16* satellite] at 1838 UTC 2 Aug, which is available online from the Naval Research Laboratory–Monterey at http://www.nrlmry.navy.mil/TC.html.

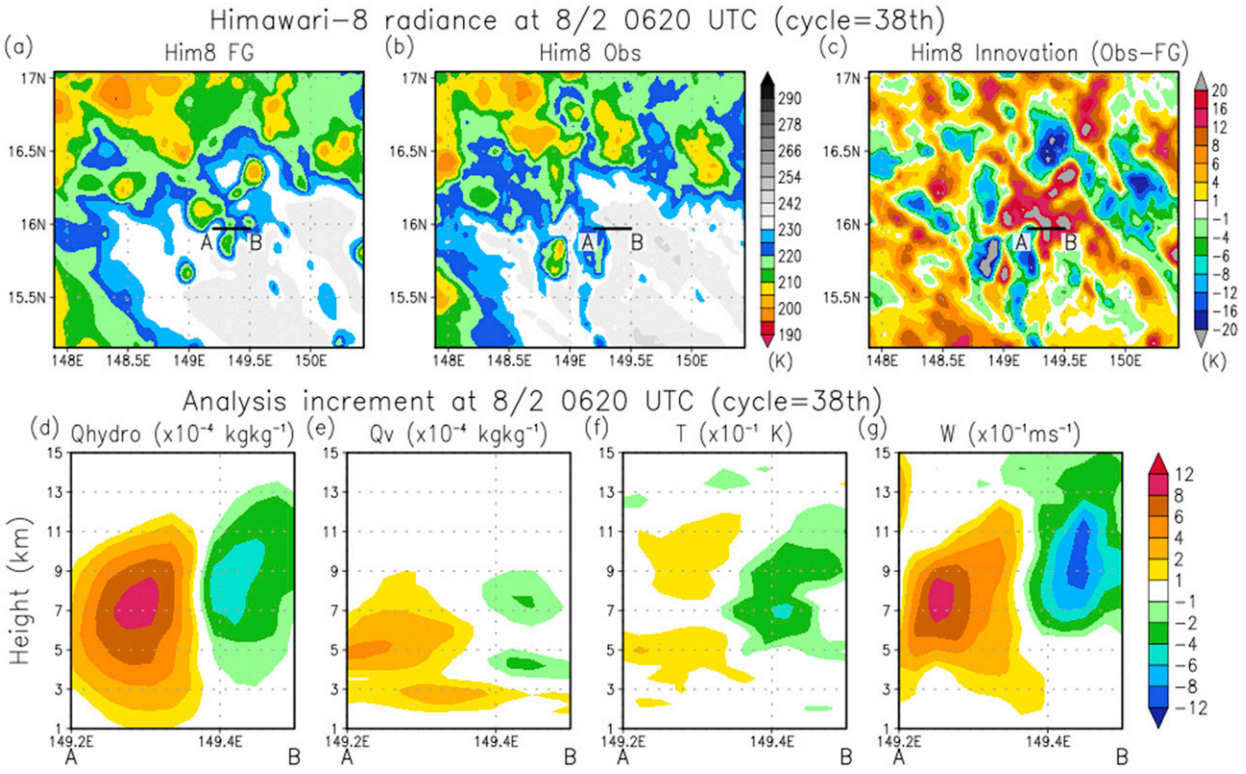

FIG. 7. (a)–(c) Horizontal maps of (a) first-guess *Himawari-8* brightness temperature, (b) actual *Himawari-8* observation, and (c) observation-minus-background innovations (K), respectively. (d)–(g) Zonal–vertical cross sections of analysis increments of (d) hydrometeors (10^{-4} kg kg^{-1}), (e) water vapor (10^{-4} kg kg^{-1}), (f) temperature (10^{-1} K), and (g) vertical velocity (10^{-1} m s^{-1}) along the A–B line in (a)–(c). The analysis time is 0620 UTC 2 Aug 2015 (38th cycle), when only the *Himawari-8* observations were assimilated.

IR radiances cannot penetrate deep clouds, so that they would not contain much direct information below the cloud top. However, such a cloud should be accompanied by a temperature anomaly due to latent heat release, low-level convergence, upward moisture transport, and production of hydrometeors. These correlations among different variables should be contained in the ensemble forecasts. Therefore, assimilating IR radiances can modify not only around the cloud top but also lower levels. To obtain more of this benefit, the vertical localization scale for all-sky IR radiances, particularly those with broad weighting functions, should be set to a larger value compared to other observations. Since a larger localization scale generally includes more sampling errors due to a limited ensemble size, we need to tune it carefully by considering these factors simultaneously.

Not only the outer rainband but also the inner core is improved by assimilating the *Himawari-8* IR. Figure 8 shows azimuthally averaged radius–height cross sections of the analyzed TCs in NoHim8 and Him8. The upper-level warm core in Him8 is stronger than that in NoHim8. Warm temperature anomaly is also found around 2–3-km levels. This is consistent with the temperature analysis increment by assimilating the *Himawari-8* IR (Fig. 7f). Some previous studies indicated the relationship between the formation of an upper-level warm core and the onset of rapid intensification (Zhang and Chen 2012; Chen and Zhang 2013). Moreover, the radius of maximum wind (RMW, shown by red marks in Figs. 8a,b) in Him8 is slightly smaller than that in NoHim8; namely, the analyzed TC in Him8 has a more contracted structure compared to that in NoHim8. Miyamoto and Takemi (2015) indicated that TCs with contracted structure have a small Rossby number and are more favorable for rapid intensification. In summary, assimilating the *Himawari-8* IR radiances can modify the overall TC structure including both the TC outer rainband and TC core regions, and can change the resulting TC development.

b. TC intensity and track forecasts

To reveal the impact of the *Himawari-8* DA on the TC forecasts, we conduct a series of deterministic forecasts initiated from the ensemble mean analysis in each experiment every hour from 1200 UTC 2 August to 0000 UTC 3 August 2015 (a total of 13 forecasts in each

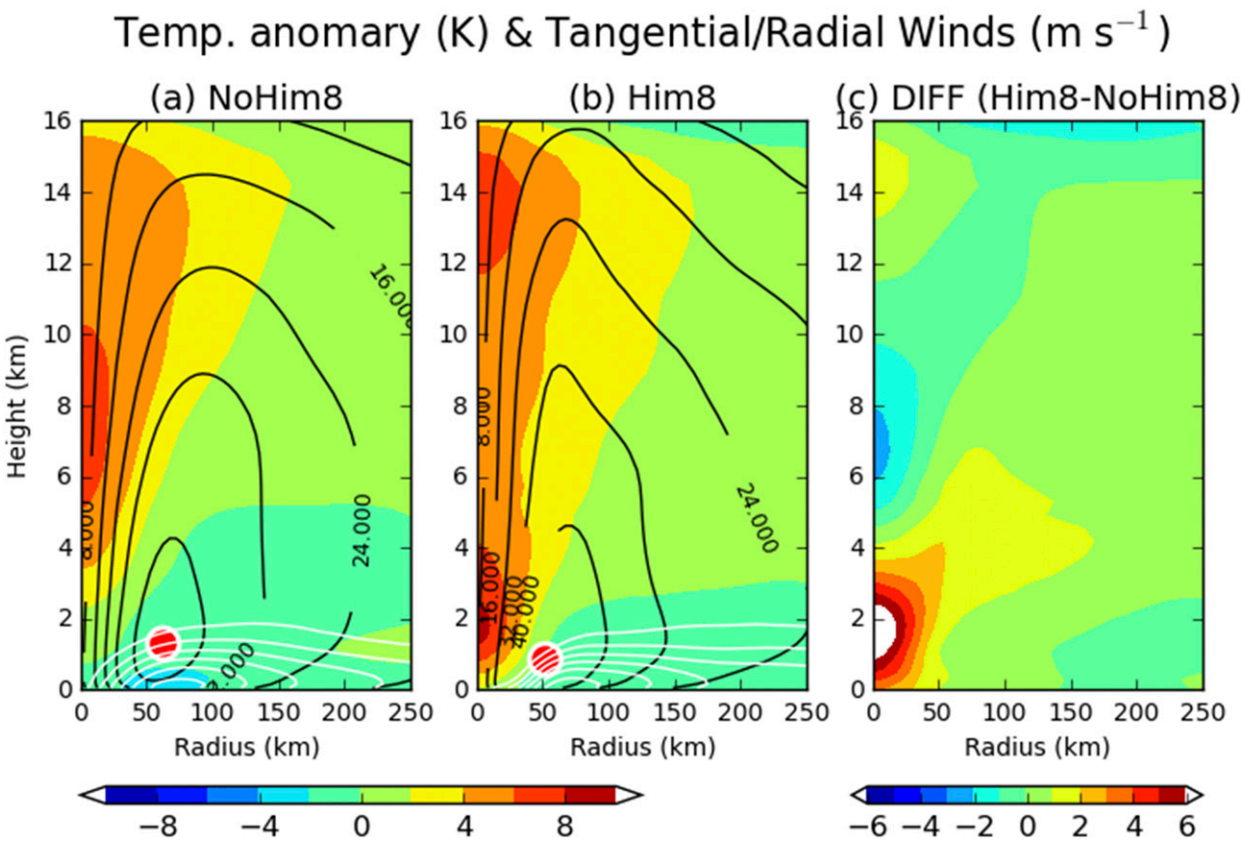

FIG. 8. (a),(b) Composites of analyzed azimuthally averaged radius–height cross sections using the (a) NoHim8 and (b) Him8 analyses at 13 different times (every hour from 1200 UTC 2 Aug to 0000 UTC 3 Aug). Color shades show temperature anomaly relative to a reference profile at a radius of 500 km. Black contours, white contours, and red marks show tangential wind velocity (m s^{-1}), radial wind velocity (m s^{-1}), and the location of the RMW in each experiment. (c) As in (a),(b), but color shades indicate the temperature anomaly difference between Him8 and NoHim8.

experiment). Figure 9 shows the evolution of the analysis and forecast TC intensities measured by the MSLP in Him8 and NoHim8. The TC intensity analysis in Him8 is closer to the best track compared to NoHim8, especially in a later period.

The TC intensity forecasts are improved by assimilating the *Himawari-8* radiances. The TC intensity forecasts in Him8 are stronger than those of NoHim8, and are closer to the best track data (Fig. 9). In both experiments, the TC forecasts from the ensemble mean exhibit spin down at the beginning of the forecasts. This is similar to the Hurricane Weather Research and Forecasting Model (HWRF) shown by Tallapragada et al. (2014). A possible remedy for this spin down issue is to use a more balanced initial condition instead of the ensemble mean (Schraff et al. 2016). After the spin down, the Him8 TCs begin to intensify quickly. In particular, a sharp deepening trend around 0300 UTC 3 August 2015 is well captured by the Him8 forecasts.

The TC intensification in Him8 would be associated with the improved TC structure in the analysis. As mentioned above, the warm core in Him8 is much stronger than that in NoHim8 (Fig. 8). In addition, the analyzed TC in Him8 had a more contracted structure and stronger initial intensity compared to NoHim8. These initial differences near the TC core region would contribute to the differences in the TC intensity forecasts. Indeed, Emanuel and Zhang (2016) addressed error sources of the TC intensity forecasts and showed that initial intensity errors dominate over environmental-flow errors in the first few days.

Another noteworthy difference in the analyzed TC inner-core region is moisture. A recent study by Emanuel and Zhang (2017) investigated the importance of the inner-core moisture and demonstrated that the initial inner-core moisture error contributes to the forecast TC intensity error within a few days, as well as the wind error. In particular, they found that the initial inner-core moisture error above the boundary layer induces large uncertainties in the

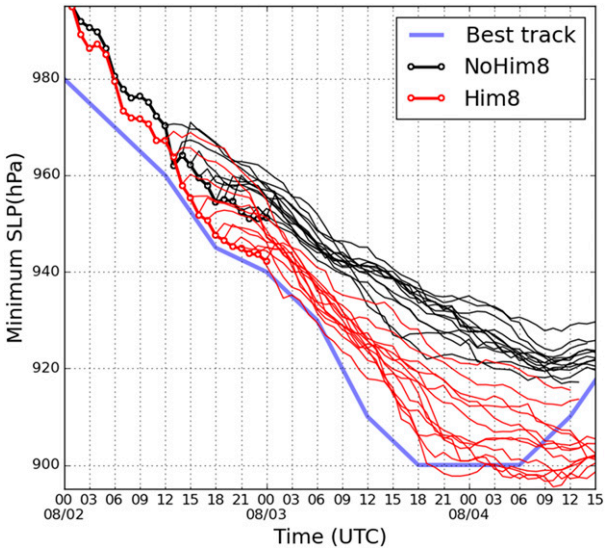

FIG. 9. Time series of minimum sea level pressure (MSLP; hPa) of Typhoon Soudelor (2015) for NoHim8 (black) and Him8 (red), respectively. The hourly analyses are shown by the thick lines with open circles. The blue line shows the 6-hourly best track data of JMA. Each thin line corresponds to forecasts from the ensemble mean analyses at different initial times (total 13 initial times every hour from 1200 UTC 2 Aug to 0000 UTC 3 Aug).

TC intensity forecast. Figure 10a shows averaged water vapor mixing ratio in the inner-core region in each experiment. Following Emanuel and Zhang (2017), the inner-core region is defined as a region within a radius of 300 km from the TC center. Him8 clearly shows more moisture in the inner-core region than NoHim8, not only below the boundary layer but also in the free troposphere. This difference would be caused by the moisture analysis increment by assimilating the *Himawari-8* observations (Fig. 7e). As shown in scatterplots in Fig. 10c, abundant moisture near the inner-core region is associated with the forecast TC intensity. In addition, *Himawari-8* DA contributed to reduce the analysis ensemble spread (uncertainty) of water vapor near the TC center (Fig. 10b). Emanuel and Zhang (2017) noted that improving moisture near the inner core by DA would give a better forecast, when observation related to inner-core humidity is available. Indeed, *Himawari-8* is that kind of observation, because it can frequently observe TCs in the western North Pacific using moisture-sensitive bands. Not only the initial intensity of the TCs, but also the inner-core moisture difference, is likely to contribute to the improvement of the TC intensity forecasts.

Clear differences in the analyses were found not only near the TC core region but also in the outer rainbands, which are well captured in Him8 (Figs. 2 and 6). Although the influence of outer rainbands on TC development has not been well understood, several studies indicated potential roles of outer rainbands. For example, May and Holland (1999) discussed that potential vorticity generation in outer rainbands might contribute to the TC development. Moreover, Wang (2009) proposed a hydrostatic adjustment mechanism in which radially dependent

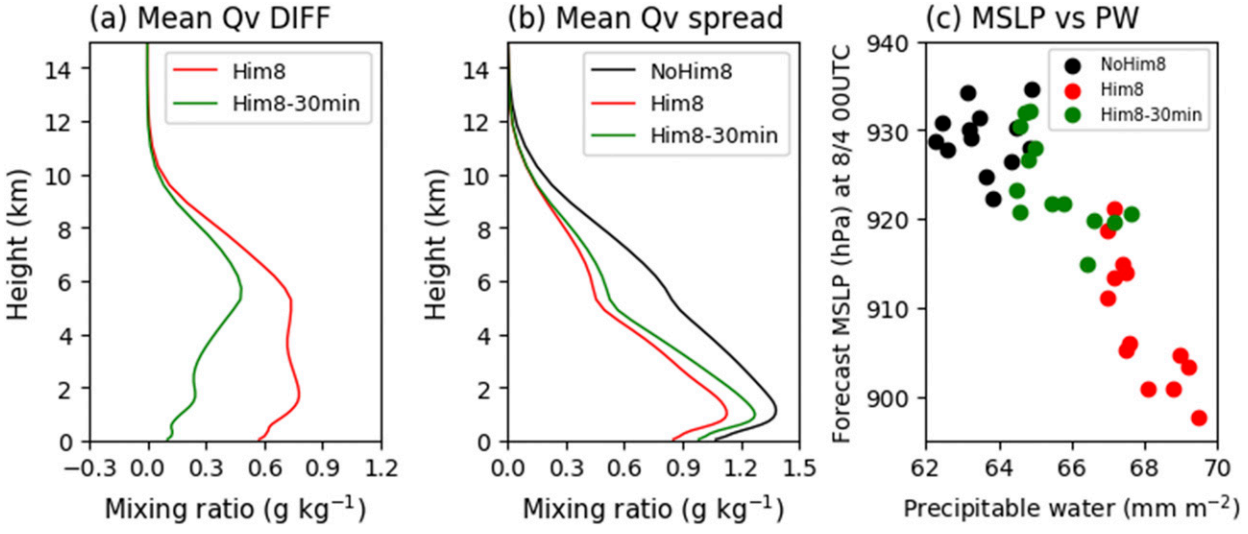

FIG. 10. (a) The vertical profiles of the inner-core (within a radius of 300 km from the TC center) averaged water vapor mixing ratio (g kg^{-1}) differences in Him8 (red curves) and Him8–30min (green curves) relative to NoHim8. A total of 13 vertical profiles obtained from hourly analyses from 1200 UTC 2 Aug to 0000 UTC 3 Aug in each experiment are averaged. (b) As in (a), but analysis ensemble spread of water vapor (g kg^{-1}). (c) Scatterplots between the analyzed precipitable water (mm m^{-2}) in the inner-core region and forecast MSLP (hPa) at 0000 UTC 4 Aug 2015 from 13 different initial times in NoHim8 (black marks), Him8 (red marks), and Him8–30min (green marks).

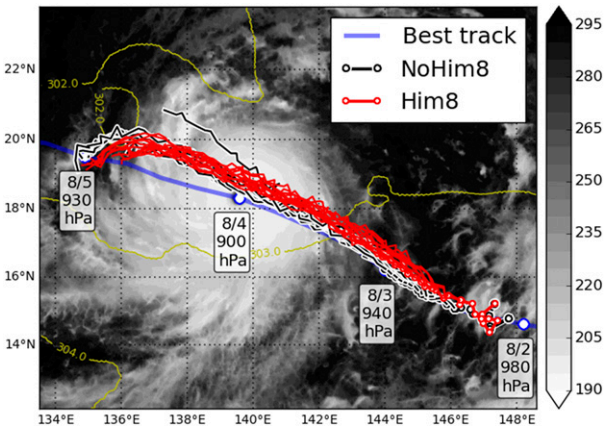

FIG. 11. Horizontal maps of the analysis and forecast TC tracks (lines), actual *Himawari-8* observation at band 13 (10.4 μm, colors), and sea surface temperature (SST, yellow contours), respectively. *Himawari-8* observation and SST are at 0000 UTC 4 Aug 2015. The analyses in each experiment are shown by the black (NoHim8) and red (Him8) thick lines with open circles. The blue line shows the 6-hourly best track estimates of JMA. Each thin line corresponds to forecasts from the ensemble mean analyses at different initial times (total 13 initial times every hour from 1200 UTC 2 Aug to 0000 UTC 3 Aug).

heating and associated SLP changes in outer rainbands affect the size and intensity of TCs. The inner-core and outer-rainband differences in the analyzed TCs may account for the TC intensification in Him8.

Figure 11 shows analysis and forecast TC tracks, and horizontal maps of actual *Himawari-8* observation and sea surface temperature (SST). NoHim8 already shows an accurate track forecast. The Him8 forecast tracks mostly overlap with those in NoHim8. In addition, there is no large SST gradient, so that the small track difference would not strongly affect the intensity forecasts. Moreover, the environmental vertical shear was similar between NoHim8 and Him8 (not shown). It is important to note that the forecast time is much shorter than Miyoshi and Kunii (2012), who demonstrated that assimilating the AIRS retrieval data improved the skill of TC track forecasts only after 48 h. Furthermore, although the TC track is in principle controlled by the large-scale general atmospheric flow (Galarneau and Davis 2013; Nakazawa and Rajendran 2007), *Himawari-8* DA in this study is limited within a narrow area. Investigating more TC cases at different stages to assess the impact of the *Himawari-8* observation on TC track forecasts would be an interesting subject of future research.

c. *Benefits of frequent DA*

An important advantage of the *Himawari-8* satellite is its high observing frequency compared to the past-generation geostationary satellites (Bessho et al. 2016). We could assimilate only every-30-min IR radiances in the Northern Hemisphere from the past-generation satellites. Namely, *Himawari-8* provides 3 times more frequent additional IR observations. Here, we aim to demonstrate this advantage by conducting an additional DA experiment with every-30-min (instead of every 10 min) *Himawari-8* observations (hereafter labeled as "Him8-30min"). In Him8–30min, the *Himawari-8* observations are assimilated every 30 min by thinning the data temporally. The conventional PREPBUFR and TC vital observations are assimilated as in the Him8 and NoHim8 experiments. The other DA configurations including covariance inflation in Him8–30min are chosen to be the same as those in Him8.

Figure 12 shows the horizontal maps of *Himawari-8* radiances simulated from the analyses in Him8–30min and Him8. In general, Him8–30min also successfully captures the observed patterns (Figs. 2 and 12). In some parts, however, the observed structure well captured by Him8 is missing in Him8–30min. For example, Him8–30min exhibits a large and clear eye of the TC at 1800 UTC 2 August 2015, albeit neither the Him8 analysis nor actual *Himawari-8* observation has such a clear eye at this developing stage (Figs. 2i and 12c,f). In addition, a northeastern part of the outer rainbands in Him8–30min is also different from the Him8 analysis and actual *Himawari-8* observation (Figs. 2 and 12).

A benefit of the frequent *Himawari-8* DA is also found in the RMSE and bias time series in Fig. 13. As expected, RMSE relative to the *Himawari-8* observations is increased in Him8–30min compared to Him8. Moreover, bias relative to the *Himawari-8* observations in Him8–30min is larger than Him8, indicating that assimilating the every-10-min *Himawari-8* observations can prevent the model state from getting far away from the observations. This is likely associated with the reason why we could get the above promising results without bias correction.

A clear difference is also found in the TC intensity forecasts. Figure 14 presents the time series of MSLP and forecast MSLP errors in each experiment. Although Him8–30min predicts slightly stronger TCs compared to NoHim8, both the predicted and analyzed TC intensities are clearly degraded compared to Him8 (Fig. 14). Interestingly, Him8–30min exhibits an intermediate feature in the moisture field as well as the forecast TC intensity (Fig. 10), indicating that assimilating the *Himawari-8* observations contributes to the improvement of the TC intensity forecasts while the every-30-min *Himawari-8* DA is not good enough.

d. *Sensitivity to localization scales*

As mentioned in section 2, we conducted a series of sensitivity experiments with different horizontal

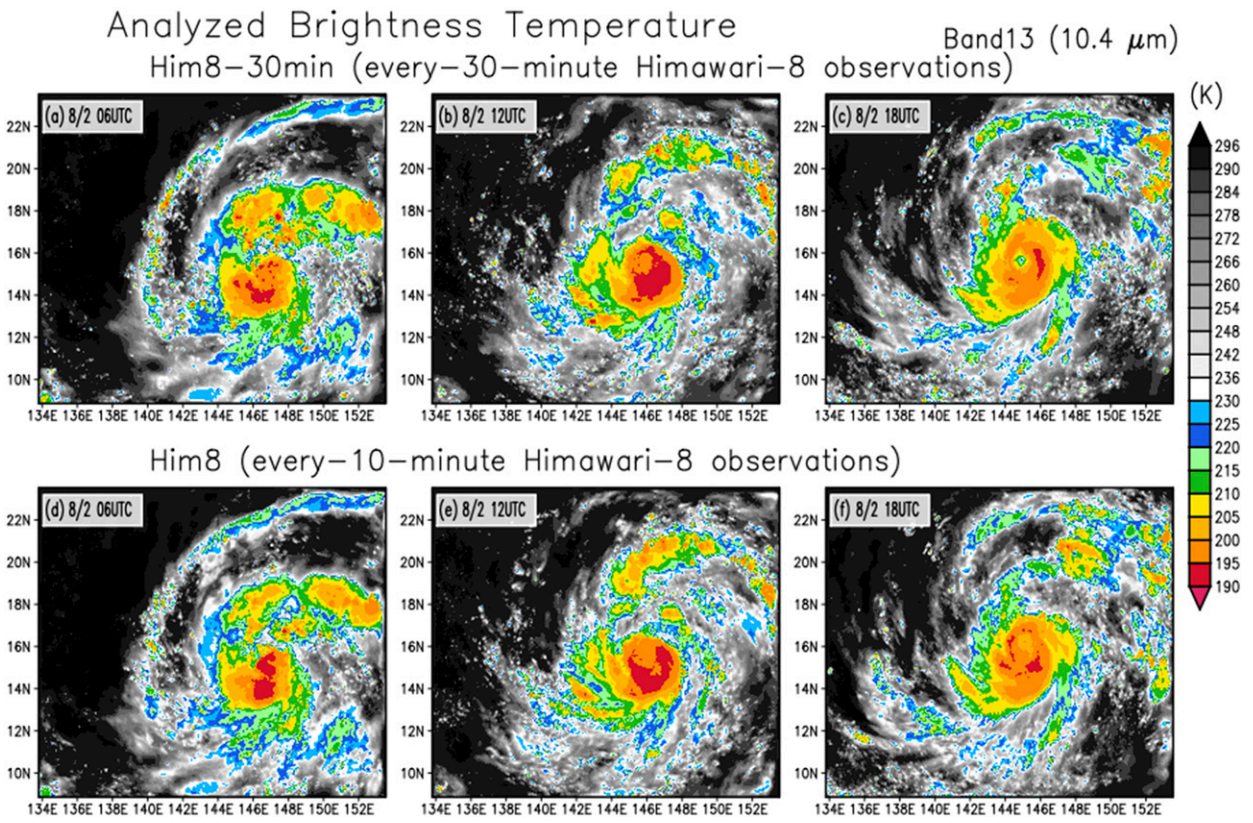

FIG. 12. As in Fig. 2, but for (a)–(c) Him8–30min and (d)–(f) Him8 at (a),(d) 0600; (b),(e) 1200; and (c),(f) 1800 UTC 2 Aug 2015.

localization scales for the *Himawari-8* observations. Figure 15 presents the time series of MSLP and forecast MSLP errors in each experiment. At the beginning, all experiments including NoHim8 exhibit spindown, similarly to other models (Tallapragada et al. 2014; Kieu and Moon 2016). In particular, the experiment with $\sigma_H = 20$ km has the worst TC intensity forecast with a strong spindown. The spindown problem is improved with larger σ_H. In addition, the analyzed TC intensity is also improved with larger σ_H. The disadvantage of using smaller σ_H would be related to the dynamical imbalance caused by narrow localization, as suggested by Kepert (2009) and Greybush et al. (2011). Figure 16 shows the forecast and analyzed TC tracks in each experiment. In contrast to the TC intensity forecasts, there is no clear sensitivity to σ_H. We also tested $\sigma_H = 70$ km but the model integration became unstable after a few tens of DA cycles, likely because of too large analysis increments and too strong wind speed in the analysis (not shown). Therefore, we concluded that $\sigma_H = 60$ km was the best choice.

4. Summary

All-sky IR observations from the new generation geostationary satellite *Himawari-8* were assimilated in a western North Pacific TC case. Innovation statistics, RMSE, and bias relative to the *Himawari-8* observation, and analysis increments showed that the *Himawari-8* DA with the SCALE-LETKF system worked correctly. The analyses were improved by assimilating the

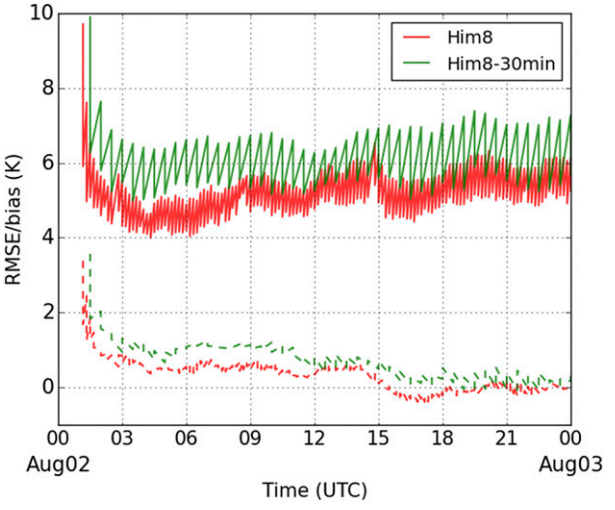

FIG. 13. As in Fig. 4, but for Him8 (red curve) and Him8–30min (green curve) at band 9 (6.9 μm).

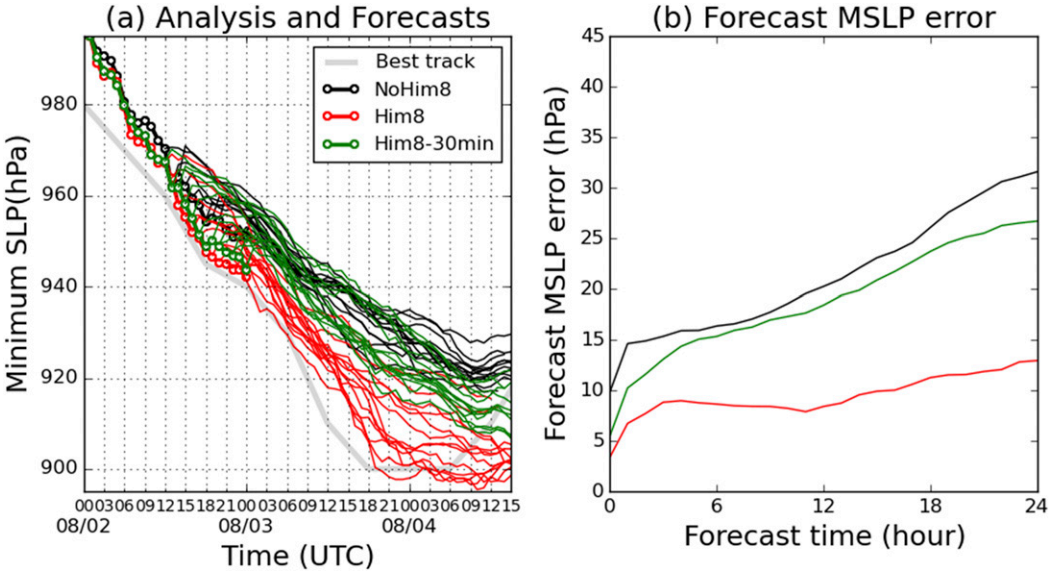

FIG. 14. (a) As in Fig. 9, but for NoHim8 (black curves), Him8 (red curves), and Him8–30min (green curves). The gray curve shows the best track. (b) Time series of the forecast MSLP errors relative to the best track averaged for 13 forecasts 1-hourly initiated from 1200 UTC 2 Aug to 0000 UTC 3 Aug 2015. The colors are as in (a).

Himawari-8 radiances every 10 min. In particular, the analyzed structure of outer rainbands was significantly improved in the radiance field and hydrometeor distribution. In addition, the analyzed TC had a strong upper-level warm core, contracted structure, and abundant moisture near the TC inner-core region.

The TC intensity forecasts were also improved by assimilating the *Himawari-8* IR radiances. This seemed to be associated with both the outer rainband and near-TC-center improvements. In particular, a clear relationship between the forecast TC intensity and initial inner-core moisture amount was observed. An additional experiment assimilating the every-30-min *Himawari-8* observations exhibited only a small improvement, indicating the advantage of every-10-min frequent DA. Moreover, the TC intensity forecasts were found to be

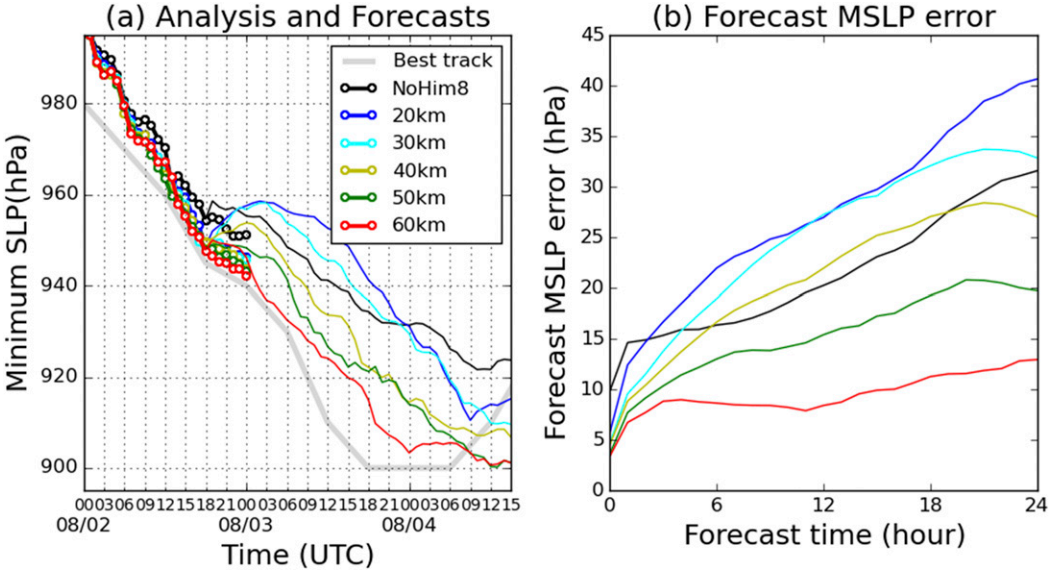

FIG. 15. As in Fig. 14, but for sensitivity experiments with the horizontal localization scale for the *Himawari-8* observations of 20 (blue), 30 (cyan), 40 (yellow), 50 (green), and 60 km (red), respectively. The gray curve shows the best track. Each thin line in (a) corresponds to forecasts from the ensemble mean analyses at 1800 UTC 2 Aug 2015.

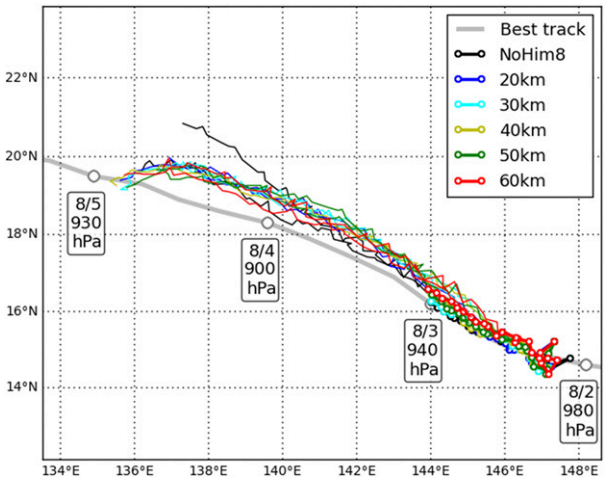

FIG. 16. As in Fig. 11, but for sensitivity experiments with the horizontal localization scale for the *Himawari-8* observations of 20 (blue), 30 (cyan), 40 (yellow), 50 (green), and 60 km (red), respectively. The gray curve shows the best track. Each thin line corresponds to forecasts from the ensemble mean analyses at two initial times (1200 and 1800 UTC 2 Aug 2015).

sensitive to the localization scale. Narrow horizontal localization caused more severe spindown of TC development, resulting in an inferior performance.

This study is the first step toward broader perspectives on the development of effective *Himawari-8* IR DA. Although we obtained promising results of assimilating the *Himawari-8* all-sky IR radiances in the single real-world TC case, this study has limitations. First, we did not consider the model and observation biases or the long-term stability of the system. Bias correction has a potential to improve the results though we observed that the bias relative to the *Himawari-8* observations was very small in this particular case. In addition, some studies showed advantages of the cloud-dependent or flow-dependent observation error for IR radiance assimilation (Okamoto et al. 2014; Harnisch et al. 2016; Minamide and Zhang 2017), while this study used a simplified approach. Also, more cases are required to examine the robustness of the impacts of assimilating the *Himawari-8* IR data on the TC forecasts. Although *Himawari-8* has 10 IR bands, only a single band 9 was assimilated. Assimilating multiple IR bands with an appropriate treatment for observation error correlations could give further improvement. We will address these issues in our future research.

Acknowledgments. The authors thank anonymous reviewers and the members of Data Assimilation Research Team, RIKEN Advanced Institute for Computational Science (AICS), for their constructive comments and useful suggestions. The *Himawari-8* radiance data were provided by the National Institute of Information and Communications Technology (NICT) Science Cloud. The NCEP PREPBUFR observation is available online from http://rda.ucar.edu/datasets/ds337.0/. The authors thank James Hocking for providing the RTTOV coefficients files of AHI. Part of the results were obtained by using computational resources of the K computer, provided by RIKEN AICS (Project ID: hp150019, hp160162, hp170178, and ra000015). This work was partly supported by JST CREST (Grants JPMJCR1312 and JPMJCR1303), FOCUS Establishing Supercomputing Center of Excellence, and FLAGSHIP2020, MEXT within the priority issue 4 "Advancement of meteorological and global environmental predictions utilizing observational 'Big Data.'" TH is the main author, performed the experiments and analyzed the results. TM is the PI and directed the research with substantial contributions to the development of the entire manuscript. GYL developed the SCALE-LETKF system and provided fundamental suggestions on data assimilation experiments. TH and GYL implemented the *Himawari-8* assimilation part into the SCALE-LETKF system. SN, RY, SAA, and HT contributed substantially on the SCALE model settings and the analysis of the results. KT and KO provided fundamental support on the implementation of the RTTOV11.2. KB provided the *Himawari-8* decoder.

REFERENCES

Bauer, P., G. Ohring, C. Kummerow, and T. Auligne, 2011: Assimilating satellite observations of clouds and precipitation into NWP models. *Bull. Amer. Meteor. Soc.*, **92**, ES25–ES28, https://doi.org/10.1175/2011BAMS3182.1.

Beljaars, A. C. M., and A. A. M. Holtslag, 1991: Flux parameterization over land surfaces for atmospheric models. *J. Appl. Meteor.*, **30**, 327–341, https://doi.org/10.1175/1520-0450(1991)030<0327:FPOLSF>2.0.CO;2.

Bessho, K., and Coauthors, 2016: An introduction to *Himawari-8/9*—Japan's new-generation geostationary meteorological satellites. *J. Meteor. Soc. Japan*, **94**, 151–183, https://doi.org/10.2151/jmsj.2016-009.

Bormann, N., A. Collard, and P. Bauer, 2010: Estimates of spatial and interchannel observation-error characteristics for current sounder radiances for numerical weather prediction. II: Application to AIRS and IASI data. *Quart. J. Roy. Meteor. Soc.*, **136**, 1051–1063, https://doi.org/10.1002/qj.615.

——, M. Bonavita, R. Dragani, R. Eremaa, M. Matricardi, and A. McNally, 2016: Enhancing the impact of IASI observations through an updated observation-error covariance matrix. *Quart. J. Roy. Meteor. Soc.*, **142**, 1767–1780, https://doi.org/10.1002/qj.2774.

Campbell, W. F., E. A. Satterfield, B. Ruston, and N. L. Baker, 2017: Accounting for correlated observation error in a dual-formulation 4D variational data assimilation system. *Mon. Wea. Rev.*, **145**, 1019–1032, https://doi.org/10.1175/MWR-D-16-0240.1.

Chen, H., and D.-L. Zhang, 2013: On the rapid intensification of Hurricane Wilma (2005). Part II: Convective bursts and the upper-level warm core. *J. Atmos. Sci.*, **70**, 146–162, https://doi.org/10.1175/JAS-D-12-062.1.

Chen, Y., and C. Snyder, 2007: Assimilating vortex position with an ensemble Kalman filter. *Mon. Wea. Rev.*, **135**, 1828–1845, https://doi.org/10.1175/MWR3351.1.

DeMaria, M., C. R. Sampson, J. A. Knaff, and K. D. Musgrave, 2014: Is tropical cyclone intensity guidance improving? *Bull. Amer. Meteor. Soc.*, **95**, 387–398, https://doi.org/10.1175/BAMS-D-12-00240.1.

Derber, J. C., and W.-S. Wu, 1998: The use of TOVS cloud-cleared radiances in the NCEP SSI analysis system. *Mon. Wea. Rev.*, **126**, 2287–2299, https://doi.org/10.1175/1520-0493(1998)126<2287:TUOTCC>2.0.CO;2.

Desroziers, G., L. Berre, B. Chapnik, and P. Poli, 2005: Diagnosis of observation, background and analysis-error statistics in observation space. *Quart. J. Roy. Meteor. Soc.*, **131**, 3385–3396, https://doi.org/10.1256/qj.05.108.

Emanuel, K. A., and F. Zhang, 2016: On the predictability and error sources of tropical cyclone intensity forecasts. *J. Atmos. Sci.*, **73**, 3739–3747, https://doi.org/10.1175/JAS-D-16-0100.1.

——, and ——, 2017: The role of inner-core moisture in tropical cyclone predictability and practical forecast skill. *J. Atmos. Sci.*, **74**, 2315–2324, https://doi.org/10.1175/JAS-D-17-0008.1.

Fertig, E. J., and Coauthors, 2009: Observation bias correction with an ensemble Kalman filter. *Tellus*, **61A**, 210–226, https://doi.org/10.1111/j.1600-0870.2008.00378.x.

Galarneau, T. J., and C. A. Davis, 2013: Diagnosing forecast errors in tropical cyclone motion. *Mon. Wea. Rev.*, **141**, 405–430, https://doi.org/10.1175/MWR-D-12-00071.1.

Greybush, S. J., E. Kalnay, T. Miyoshi, K. Ide, and B. R. Hunt, 2011: Balance and ensemble Kalman filter localization techniques. *Mon. Wea. Rev.*, **139**, 511–522, https://doi.org/10.1175/2010MWR3328.1.

Harnisch, F., M. Weissmann, and Á. Periáñez, 2016: Error model for the assimilation of cloud-affected infrared satellite observations in an ensemble data assimilation system. *Quart. J. Roy. Meteor. Soc.*, **142**, 1797–1808, https://doi.org/10.1002/qj.2776.

Heming, J. T., 2016: Met Office unified model tropical cyclone performance following major changes to the initialization scheme and a model upgrade. *Wea. Forecasting*, **31**, 1433–1449, https://doi.org/10.1175/WAF-D-16-0040.1.

Holt, C., I. Szunyogh, G. Gyarmati, S. M. Leidner, and R. N. Hoffman, 2015: Assimilation of tropical cyclone observations: Improving the assimilation of TCVitals, scatterometer winds, and dropwindsonde observations. *Mon. Wea. Rev.*, **143**, 3956–3980, https://doi.org/10.1175/MWR-D-14-00158.1.

Honda, T., S. Kotsuki, G.-Y. Lien, Y. Maejima, K. Okamoto, and T. Miyoshi, 2018: Assimilation of *Himawari-8* all-sky radiances every 10 minutes: Impact on precipitation and flood risk prediction. *J. Geophys. Res.*, https://doi.org/10.1002/2017JD027096, in press.

Houtekamer, P. L., H. L. Mitchell, G. Pellerin, M. Buehner, M. Charron, L. Spacek, and B. Hansen, 2005: Atmospheric data assimilation with an ensemble Kalman filter: Results with real observations. *Mon. Wea. Rev.*, **133**, 604–620, https://doi.org/10.1175/MWR-2864.1.

Hsiao, L.-F., C.-S. Liou, T.-C. Yeh, Y.-R. Guo, D.-S. Chen, K.-N. Huang, C.-T. Terng, and J.-H. Chen, 2010: A vortex relocation scheme for tropical cyclone initialization in Advanced Research WRF. *Mon. Wea. Rev.*, **138**, 3298–3315, https://doi.org/10.1175/2010MWR3275.1.

Hunt, B. R., E. J. Kostelich, and I. Szunyogh, 2007: Efficient data assimilation for spatiotemporal chaos: A local ensemble transform Kalman filter. *Physica D*, **230**, 112–126, https://doi.org/10.1016/j.physd.2006.11.008.

Kepert, J. D., 2009: Covariance localisation and balance in an ensemble Kalman filter. *Quart. J. Roy. Meteor. Soc.*, **135**, 1157–1176, https://doi.org/10.1002/qj.443.

Kieu, C. Q., and Z. Moon, 2016: Hurricane intensity predictability. *Bull. Amer. Meteor. Soc.*, **97**, 1847–1857, https://doi.org/10.1175/BAMS-D-15-00168.1.

Kleist, D. T., 2011: Assimilation of tropical cyclone advisory minimum sea level pressure in the NCEP global data assimilation system. *Wea. Forecasting*, **26**, 1085–1091, https://doi.org/10.1175/WAF-D-11-00045.1.

Kunii, M., 2015: Assimilation of tropical cyclone track and wind radius data with an ensemble Kalman filter. *Wea. Forecasting*, **30**, 1050–1063, https://doi.org/10.1175/WAF-D-14-00088.1.

Kusaka, H., H. Kondo, Y. Kikegawa, and F. Kimura, 2001: A simple single-layer urban canopy model for atmospheric models: Comparison with multi-layer and slab models. *Bound.-Layer Meteor.*, **101**, 329–358, https://doi.org/10.1023/A:1019207923078.

Lei, L., and J. S. Whitaker, 2015: Model space localization is not always better than observation space localization for assimilation of satellite radiances. *Mon. Wea. Rev.*, **143**, 3948–3955, https://doi.org/10.1175/MWR-D-14-00413.1.

Lien, G.-Y., T. Miyoshi, S. Nishizawa, R. Yoshida, H. Yashiro, S. A. Adachi, T. Yamaura, and H. Tomita, 2017: The near-real-time SCALE-LETKF system: A case of the September 2015 Kanto-Tohoku heavy rainfall. *SOLA*, **13**, 1–6, https://doi.org/10.2151/sola.2017-001.

Lin, H., S. Weygandt, S. Benjamin, and M. Hu, 2017: Satellite radiance data assimilation with the hourly updated rapid refresh. *Wea. Forecasting*, **32**, 1273–1287, https://doi.org/10.1175/WAF-D-16-0215.1.

May, P. T., and G. J. Holland, 1999: The role of potential vorticity generation in tropical cyclone rainbands. *J. Atmos. Sci.*, **56**, 1224–1228, https://doi.org/10.1175/1520-0469(1999)056<1224:TROPVG>2.0.CO;2.

Minamide, M., and F. Zhang, 2017: Adaptive observation error inflation for assimilating all-sky satellite radiance. *Mon. Wea. Rev.*, **145**, 1063–1081, https://doi.org/10.1175/MWR-D-16-0257.1.

Miyamoto, Y., and T. Takemi, 2015: A triggering mechanism for rapid intensification of tropical cyclones. *J. Atmos. Sci.*, **72**, 2666–2681, https://doi.org/10.1175/JAS-D-14-0193.1.

Miyoshi, T., and Y. Sato, 2007: Assimilating satellite radiances with a local ensemble transform Kalman filter (LETKF) applied to the JMA global model (GSM). *SOLA*, **3**, 37–40, https://doi.org/10.2151/sola.2007-010.

——, and S. Yamane, 2007: Local ensemble transform Kalman filtering with an AGCM at a T159/L48 resolution. *Mon. Wea. Rev.*, **135**, 3841–3861, https://doi.org/10.1175/2007MWR1873.1.

——, and M. Kunii, 2012: Using AIRS retrievals in the WRF-LETKF system to improve regional numerical weather prediction. *Tellus*, **64A**, 18408, https://doi.org/10.3402/tellusa.v64i0.18408.

——, Y. Sato, and T. Kadowaki, 2010: Ensemble Kalman filter and 4D-Var intercomparison with the Japanese operational global analysis and prediction system. *Mon. Wea. Rev.*, **138**, 2846–2866, https://doi.org/10.1175/2010MWR3209.1.

Nakanishi, M., and H. Niino, 2004: An improved Mellor–Yamada level-3 model with condensation physics: Its design and verification. *Bound.-Layer Meteor.*, **112**, 1–31, https://doi.org/10.1023/B:BOUN.0000020164.04146.98.

Nakazawa, T., and K. Rajendran, 2007: Relationship between tropospheric circulation over the western North Pacific and tropical cyclone approach/landfall on Japan. *J. Meteor. Soc. Japan*, **85**, 101–114, https://doi.org/10.2151/jmsj.85.101.

National Hurricane Center, 2016: National Hurricane Center forecast verification. National Hurricane Center, accessed 15 September 2016, http://www.nhc.noaa.gov/verification/.

Nehrkorn, T., B. K. Woods, R. N. Hoffman, and T. Auligné, 2015: Correcting for position errors in variational data assimilation. *Mon. Wea. Rev.*, **143**, 1368–1381, https://doi.org/10.1175/MWR-D-14-00127.1.

Nishizawa, S., H. Yashiro, Y. Sato, Y. Miyamoto, and H. Tomita, 2015: Influence of grid aspect ratio on planetary boundary layer turbulence in large-eddy simulations. *Geosci. Model Dev.*, **8**, 3393–3419, https://doi.org/10.5194/gmd-8-3393-2015.

Okamoto, K., 2017: Evaluation of IR radiance simulation for all-sky assimilation of *Himawari-8*/AHI in a mesoscale NWP system. *Quart. J. Roy. Meteor. Soc.*, **143**, 1517–1527, https://doi.org/10.1002/qj.3022.

——, A. P. McNally, and W. Bell, 2014: Progress towards the assimilation of all-sky infrared radiances: An evaluation of cloud effects. *Quart. J. Roy. Meteor. Soc.*, **140**, 1603–1614, https://doi.org/10.1002/qj.2242.

Otkin, J. A., 2012: Assimilation of water vapor sensitive infrared brightness temperature observations during a high impact weather event. *J. Geophys. Res.*, **117**, D19203, https://doi.org/10.1029/2012JD017568.

——, W. E. Lewis, A. J. Lenzen, B. D. McNoldy, and S. J. Majumder, 2017: Assessing the accuracy of the cloud and water vapor fields in the Hurricane WRF (HWRF) Model using satellite infrared brightness temperatures. *Mon. Wea. Rev.*, **145**, 2027–2046, https://doi.org/10.1175/MWR-D-16-0354.1.

Qin, Z., X. Zou, and F. Weng, 2017: Impacts of assimilating all or GOES-like AHI infrared channels radiances on QPFs over Eastern China. *Tellus*, **69A**, 1345265, https://doi.org/10.1080/16000870.2017.1345265.

Sato, Y., S. Nishizawa, H. Yashiro, Y. Miyamoto, Y. Kajikawa, and H. Tomita, 2015: Impacts of cloud microphysics on trade wind cumulus: Which cloud microphysics processes contribute to the diversity in a large eddy simulation? *Prog. Earth Planet. Sci.*, **2**, 23, https://doi.org/10.1186/s40645-015-0053-6.

Saunders, R., and Coauthors, 2013: RTTOV-11: Science and validation report. NWP-SAF Rep. NWPSAF-MO-TV-032, Met Office, United Kingdom, 62 pp., https://nwpsaf.eu/oldsite/deliverables/rtm/docs_rttov11/rttov11_svr.pdf.

Schraff, C., H. Reich, A. Rhodin, A. Schomburg, K. Stephen, A. Periáñez, and R. Potthast, 2016: Kilometre-scale ensemble data assimilation for the COSMO model (KENDA). *Quart. J. Roy. Meteor. Soc.*, **142**, 1453–1472, https://doi.org/10.1002/qj.2748.

Sekiguchi, M., and T. Nakajima, 2008: A k-distribution-based radiation code and its computational optimization for an atmospheric general circulation model. *J. Quant. Spectrosc. Radiat. Transfer*, **109**, 2779–2793, https://doi.org/10.1016/j.jqsrt.2008.07.013.

Tallapragada, V., C. Kieu, Y. Kwon, S. Trahan, Q. Liu, Z. Zhang, and I.-H. Kwon, 2014: Evaluation of storm structure from the operational HWRF during 2012 implementation. *Mon. Wea. Rev.*, **142**, 4308–4325, https://doi.org/10.1175/MWR-D-13-00010.1.

Tomita, H., 2008: New microphysical schemes with five and six categories by diagnostic generation of cloud ice. *J. Meteor. Soc. Japan*, **86**, 121–142, https://doi.org/10.2151/jmsj.86A.121.

Torn, R. D., 2010: Performance of a mesoscale ensemble Kalman filter (EnKF) during the NOAA high-resolution Hurricane test. *Mon. Wea. Rev.*, **138**, 4375–4392, https://doi.org/10.1175/2010MWR3361.1.

——, and C. Snyder, 2012: Uncertainty of tropical cyclone best-track information. *Wea. Forecasting*, **27**, 715–729, https://doi.org/10.1175/WAF-D-11-00085.1.

Velden, C., and Coauthors, 2006: The Dvorak tropical cyclone intensity estimation technique: A satellite-based method that has endured for over 30 years. *Bull. Amer. Meteor. Soc.*, **87**, 1195–1210, https://doi.org/10.1175/BAMS-87-9-1195.

Wang, Y., 2009: How do outer spiral rainbands affect tropical cyclone structure and intensity? *J. Atmos. Sci.*, **66**, 1250–1273, https://doi.org/10.1175/2008JAS2737.1.

Wu, C.-C., G.-Y. Lien, J.-H. Chen, and F. Zhang, 2010: Assimilation of tropical cyclone track and structure based on the ensemble Kalman filter (EnKF). *J. Atmos. Sci.*, **67**, 3806–3822, https://doi.org/10.1175/2010JAS3444.1.

——, S.-G. Chen, C.-C. Yang, and P.-H. Lin, 2012: Potential vorticity diagnosis of the factors affecting the track of Typhoon Sinlaku (2008) and the impact from dropwindsonde data during T-PARC. *Mon. Wea. Rev.*, **140**, 2670–2688, https://doi.org/10.1175/MWR-D-11-00229.1.

Zhang, D.-L., and H. Chen, 2012: Importance of the upper-level warm core in the rapid intensification of a tropical cyclone. *Geophys. Res. Lett.*, **39**, L02806, https://doi.org/10.1029/2011GL050578.

Zhang, F., and Y. Weng, 2015: Predicting hurricane intensity and associated hazard: A five-year real-time forecast experiment with assimilation of airborne Doppler radar observations. *Bull. Amer. Meteor. Soc.*, **96**, 25–33, https://doi.org/10.1175/BAMS-D-13-00231.1.

——, C. Snyder, and J. Sun, 2004: Impacts of initial estimate and observation availability on convective-scale data assimilation with an ensemble Kalman filter. *Mon. Wea. Rev.*, **132**, 1238–1253, https://doi.org/10.1175/1520-0493(2004)132<1238:IOIEAO>2.0.CO;2.

——, M. Minamide, and E. Clothiaux, 2016: Potential impacts of assimilating all-sky infrared satellite radiances from GOES-R on convection-permitting analysis and prediction of tropical cyclones. *Geophys. Res. Lett.*, **43**, 2954–2963, https://doi.org/10.1002/2016GL068468.

Zou, X., Z. Qin, and Y. Zheng, 2015: Improved tropical storm forecasts with *GOES-13/15* imager radiance assimilation and asymmetric vortex initialization in HWRF. *Mon. Wea. Rev.*, **143**, 2485–2505, https://doi.org/10.1175/MWR-D-14-00223.1.

——, X. Zhuge, and F. Zheng, 2016: Characterization of bias of Advanced Himawari Imager infrared observations from NWP background simulations using CRTM and RTTOV. *J. Atmos. Oceanic Technol.*, **33**, 2553–2567, https://doi.org/10.1175/JTECH-D-16-0105.1.